Remote sensing and in situ measurement of a supraglacial melt pond in East Greenland

William A. Sneed,[1] Gordon S. Hamilton[1]

[1] *Climate Change Institute, University of Maine, 303 Bryand Global Sciences Center, Orono, ME 04469-5790, USA*

ABSTRACT. In situ measurements of water depth and optical properties of a melt pond in eastern Greenland were collected to verify a previously developed algorithm for determining supraglacial water depths using satellite imagery. The algorithm made five simplifying assumptions that were tested using the in situ data and laboratory analyses water samples. We conclude that two were justified, one was not, and remaining two require further study, but probably have a minor effect in retrieved water depths and volumes. Measured water depths of 0.2 to 3.0 meters agree well with those derived from a satellite image using the algorithm. Numerically modeled depths also agree well with those from the satellite image. This new analysis demonstrates the validity of our algorithm as a means for determining meltwater volumes in supraglacial ponds and lakes.

INTRODUCTION

Between 1993 and 2003 Greenland contributed 0.21±0.07 mm yr^{-1} to global mean sea level rise (Lemke and others, 2007). This contribution is projected to increase to 0.3–1.9 mm yr^{-1} for the period 2090–2099 (Meehl and others, 2007). While some of the present and projected contribution is from direct meltwater runoff most of the contribution is due to changes in ice dynamics, namely faster flow velocities of outlet glaciers, and the resultant increase in the calving of solid ice into the oceans. Enhanced surface meltwater generation can play a role in these flow speed accelerations via increased subglacial lubrication facilitated by larger amounts of water reaching the bed (Parizek and Alley, 2004; Boon and Sharp, 2003; Van der Veen, 2007; Das and others, 2008; Bartholomew and others, 2010). Observational evidence supports this process (Zwally and others, 2002; Shepherd and others, 2009; Van de Wal and others, 2008) although its effect on outlet glacier speeds is unclear (Joughin and others, 2008). Our understanding of this complex process is limited, in part, by our knowledge of the

minimum quantity of meltwater needed, and the timing of its availability, to initiate and sustain increased glacier flow rates (Parizek and Alley, 2004).

We previously developed a method for determining the depth and, hence, the volume of surface melt ponds by applying a radiative transfer model to multi-spectral Advanced Spaceborne Thermal Emission and Reflection Radiometer (ASTER) (Sneed and Hamilton, 2007). In principal, the algorithm can also be applied to other types of visible imagery, such as Landsat 7 Enhanced Thematic Mapper Plus (Landsat 7 ETM+), and Moderate Resolution Imaging Spectroradiometer (MODIS) satellite sensor images. The bands of interest are VNIR1 (520-600 nm) and VNIR3N (780-860 nm) for ASTER; Band 2 (525-605 nm) and Band 4 (750-900 nm) for Landsat 7; and Band 4 (545-565 nm) and Band 2 (841-876 nm) for MODIS. The method used for extracting water depth and bottom albedo is based on Bouguer-Lambert-Beer's law

$$I(z,\lambda) = I(0,\lambda)e^{-(K_\lambda)(z)}, \tag{1}$$

where $I(z,\lambda)$ is the water-leaving spectral intensity at some depth, $I(0,\lambda)$ is the spectral intensity at zero depth, K_λ is the spectral attenuation, and z is depth. Written in terms of reflectance and inverted to logarithmic form (Philpot, 1989)

$$z = (ln(A_d - R_\infty) - ln(R_w - R_\infty))/(-g), \tag{2}$$

where A_d is the bottom or substrate albedo (reflectance), R_∞ is the reflectance for optically deep water, and R_w is the reflectance of some pixel-of-interest. As a practical matter, R_∞ (Eq. 2) is reflectance from optically deep water where the influence of bottom reflectance is nil and can be derived from water that is deeper than ∼40 m. With values for R_∞, g, and R_w in hand, A_d must be determined before the water depth, z, of the pixel-of-interest can be calculated. Details of the procedure for determining A_d are found in Sneed and Hamilton (2007, section 2.3).

The depth retrieval algorithm contains several simplifying assumptions listed below:

1. Suspended or dissolved, organic or inorganic, particulate matter is minimal.

2. There is no wind and, thus, no waves on a pond's surface.

3. There is no inelastic scattering, e.g., Raman scattering or flouresence.

4. The substrate of a melt pond is homogeneous.

An additional unstated assumption in Sneed and Hamilton (2007) is that the image containing surface melt water and melt ponds must also contain optically deep water suitable for deriving R_∞. In practice,this means that suitable images must cover

both the ice sheet margin and adjacent regions of ice-free ocean, a potential limitation for ASTER which are only 65 km x 65 km.

Here, we examine the validity of the above assumptions based on new theoretical analyses and field observations on an East Greenland melt pond in July 2008.

HELHEIM GLACIER, EASTERN GREENLAND

In situ data

On 11 July 2008 we carried out a depth survey of a melt pond on Helheim Glacier from a rowed, inflatable boat with simultaneous radiometric and global positioning (GPS) measurements. A digital fathometer with a measured accuracy of 0.03 m was used to collect water depths and a Garmin® handheld GPS provided position coordinates. A Satlantic Profiler II®(Satlantic, Inc., Halifax, N.S., Canada) with two hyperspectral radiometers (operated in the surface mode) was used to collect above- and below-water radiometric data. The downwelling surface irradiance radiometer with a cosine detector was positioned ∼15 cm above the water surface while the upwelling, water-leaving radiance radiometer was positioned ∼10 cm below the water surface. The radiometers were towed 5–10m behind the boat and every effort was made to not cast a shadow on the pond bottom below the radiometers. Depth and GPS data were recorded by hand and radiometric data were collected on a laptop computer. The physical configuration of the ProfilerII® precluded gathering radiometric data in water shallower than ∼0.5 m, although depth and GPS measurements were made in shallow water.

Measurements began at 1251 local time (UTC-2) and ended at 1341 local time (UTC-2). There was no detectable wind, the pond surface was calm, and the sky was clear except for a few scattered, high clouds. Our somewhat meandering course covered a straight line distance of ∼200 m on the long axis of the pond and we recorded 21 depths and 3 GPS positions. The shallowest depth of 0.7 m was recorded near 66.46231°N, 038.45100°W (524465.0E, 7371604.0N UTM 24N) and the deepest depth of 3.0 m recorded near 66.46145°N, 038.44996°W (524512.0E, 7371454.0N UTM 24N). It should be noted that our deepest recorded depth was not necessarily the deepest part of the pond. We also observed a number of scattered cryoconite holes in the pond bottom that appeared to be ∼5–15 cm in diameter. An examination of more than 3600 upwelling radiance ($L_w(0^-)$) values at 475 nm and 555 nm shows occasional sudden and temporally short decreases which probably indicate cryoconite holes.

Satellite-derived data

A satellite image from the Advanced Land Observing Satellite (ALOS, 10 m spatial resolution) for 22 June 2008 shows a roughly elliptical pond with a major axis of ∼1200 m oriented in a northwest-southeast direction and a minor axis of ∼500 m. An ASTER image of 03 August 2008 shows the pond reduced to scattered segments; the area where the in situ data of July 11th was collected completely devoid of water. However, a Landsat 7 (30 m spatial resolution) image of 20 July 2008

(path\row, 232\013) does contain the pond segment we measured on July 11th (Figure 2) and was used to calculate water depths using Equation 2. Another Landsat 7 image of July 20th (path\row, 232\014) provided the R_∞ data.

Both images were subsetted to speed-up processing, converted to top-of-atmosphere reflectance (Irish, 1999), and atmospherically corrected using the 6SV radiative transfer modeling code of Vermote and others (2005). Then following the procedures set out in Sneed and Hamilton (2007, section 2.3) water depths in the subimage were calculated (Figure 3). Because of the large spatial resolution of the Landsat image it is not possible to attribute a measured depth at a particular location with particular pixel in Figure 3. However, the depth map does show decreasing depths at the northwest and southeast end of the pond and a deep area near the middle all of which are consistent with the depths we measured at those locations.

ASSUMPTIONS

Suspended and dissolved matter

Meltwater samples were recovered from a melt pond on Helheim Glacier in July 2007 and July 2008 for detailed optical and chemical analyses. The melt pond lies about 100 km inland from the Atlantic Ocean at an elevation of ∼600 m and is equidistant (∼3 km) from two large nunataks. Not surprisingly, ion chromotography analysis of the water shows a strong marine influence. Methanesulfonate (MS^-) is present, (2.12 and 0.40 μgL^{-1}, in the 2007 and 2008 samples, repectively) and is an indirect product of marine biota (Legrand and Mayewski, 1997). The sodium (Na^+) and chloride (Cl^-) ratios for both years (0.545 and 0.515) are close to the seawater ratio, 0.557 (salinity, S=35 PSU) (Pilson, 1998) are a further indication of a marine source. The concentrations of the other major ions (K^+, Mg^{2+}, Ca^{2+}, $NO_3{}^-$, and $SO_4{}^{2-}$) are consistent with the minimum concentrations found in snow throughout the Arctic. The calcium (Ca^{2+}), potassium (K^+), and magnesium (Mg^{2+}) are most likely derived from terrestrial dust while the $NO_3{}^-$ and $SO_4{}^{2-}$ are linked to human activities (Legrand and Mayewski, 1997; de Caritat and others, 2005). The concentrations of K^+ and Mg^{2+} for both years are near the instrumental detection limit and are commensurate with the low levels of particulate scattering measured by the optical analyses below.

For the optical analyses, spectral transmittance and spectral absorption were measured at nine wavelengths using a WETLabs (Philomath, OR, USA) ac-9® absorption and attenuation meter. The spectral absorption coefficient, a and the spectral beam attentuation coefficient, c are derived from the ac-9 measurements. The ac-9 samples nine bands but we are primarily intrested in the one centered at 555 nm because it is very near the midpoints of the ASTER, Landsat, and MODIS bands used to calculate water depth.

Absorption coefficient, a, particulate and dissolved, are near the instrument's resolution limits, $a = 0.003$ and $0.010\ m^{-1}$ at 555 nm for 2007 and 2008 respectively. Particulate scattering, b, is not measured directly but derived from the energy equation, $c = a + b$. The scattering coefficients are $b = 0.050\ m^{-1}$ and $b = 0.014\ m^{-1}$ at 555 nm, 2007 and 2008 repectively. By way

of comparison, Smith and Baker (1981) analyzed freshwater from Crater Lake, Oregon, U.S.A., and reported $a = 0.0638$ m^{-1} and $b = 0.0015$ m^{-1} at 550 nm while Davies-Colley (1983) reported on three shallow lakes in New Zealand with absorption coefficients, a, of ∼0.5–∼1.4 m^{-1} and scattering coefficients, b, of 3.2–30 m^{-1} at 550 nm.

The slopes of the spectral scattering curves for both years are very similar as are the slopes of the concomitant particle size distribution curves (Boss and others, 2001) indicating that the bulk of the particulate matter has a distribution similar to that of small particles (Babin and others, 2003). Babin and others (2003) showed the close relationship between an increasing backscattering coefficient and an increase of suspended particulate matter measured by dry weight per unit volume of seawater, gm^{-3}. A similar relation should hold for backscatter coefficient and particle load in a freshwater melt pond so that any bias introduced by particulates in the calculated water depth will be minimal given the small measured values of a and b in our samples.

Wind and Waves

Quantifying the effects of wind and the resultant waves on the water depth calculated using Equation 2, requires that we know the wind speed in the area of the melt pond. The large size (>1 km in diameter) of some ponds introduces the possibility that light could be specularly reflected from a wave facet to the satellite sensor producing sunglint given the required confluence of solar and sensor relative azimuth, wind speed, wind direction, and wave facet slope. This is an unlikely scenario for most of the ice sheet so instead we take a modeling approach. Consider a circular pond with a diameter of 1 km and an idealized uniform depth of 15 m. It is possible to calculate wave amplitudes for a given wind speed, water depth, and fetch from first principles, e.g., `http://woodshole.er.usgs.gov/staffpages/csherwood/sedx_equations/RunSPMWave.html` (Table 1).

Zaneveld and others (2001) modeled remote sensing reflectance (R_{rs}) as function of wave amplitude and the angle between the light source and the sensor at a small fixed wavelength, 0.01 m. A conservative value for this angle using an ASTER image would be 5 degrees. Given the first four wave amplitudes in Table 1 and a look-angle of 5°, R_{rs} would increase by ∼5% with a 20 m^{-1} wind and, with the last set of values, R_{rs} might increase by 10–11% (Zaneveld and others, 2001, Figure 3). As the period and wavelength increase beyond the small value used by Zaneveld and others (2001) we expect the wave effect on remote sensing reflectance (and other apparent optical properties) to diminish due to spatial averaging. To test the sensitivity of remote sensing reflectance to surface wind speed five modeling runs where done using HYDROLIGHT®. We varied the wind speed between 0 ms^{-1} and 14.9 ms^{-1}, the maximum allowed by the software, while holding all other input parameters fixed and observed only a 1.4% decrease in the remote sensing reflectance. Thus, we can conclude that the effect of waves on the optical signal at the satellite, and derived water depths, is relatively unimportant.

Inelastic scattering

There is always inelastic scattering of light by natural waters (salt or fresh) at visible wavelengths. Molecular or Raman scattering is always present and fluorescence, due to dissolved or suspended organic material, can also occur. As particulate matter (organic or inorganic) decreases the effects of elastic scattering on the in-water and above-water light fields diminishes and scattering is mainly by inelastic collisions. As fluorescense decreases, the contribution of Raman scattering to the light field becomes more pronounced (e.g., Morel and Gentili, 1991; Morel and Loisel, 1998). But, as Gordon (1999) points out, Raman scattering in natural waters is relevant to the remote sensing of ocean color and its use as a proxy for oceanic biological productivitiy. Here, our interest is much simpler — to determine the depth of a glacial melt pond — and it is not necessary to partition the bulk scattering coefficient between elastic and inelastic collisions.

Substrate homogeneity

We originally assumed that the bottom of a melt pond or meltwater channel was ice with the same albedo throughout. However, we observed numerous cryoconite holes (∼5–15 cm in diameter) in the bottom of the Helheim Glacier melt pond. These holes raised the possibility that larger areas of cryoconite might collect in the deepest parts of a pond or at the bends of a meltwater channel where water velocity slows. Detecting such areas and then quantifying their effect of on calculated water depth is not trivial although the latter is the easier of the two problems.

Gadja (1958) described cryoconite as a fine or very fine dark, windblown dust composed of organic, inorganic, or both, material deposited on snow or ice surfaces and Gerdel and Drouet (1960) described the color as dark brown to blue-black. Takeuchi (2002a) analyzed cryoconite from nine glaciers, three in the Himalaya, three in Tibet, one on Baffin Island, one on Axel Heiberg, and one on Spitsbergen, for organic and mineral content and spectral reflectance. Takeuchi and colleagues have also measured the spectral reflectance (albedo) of cryoconite in such diverse regions as Patagonia (Takeuchi and others, 2001), China (Takeuchi and Li, 2008), and Alaska (Takeuchi, 2002b; Takeuchi and others, 2003). Bøggild and others (2010) have measured the spectral albedo of surface cryoconite in northeast Greenland and their values agree well with those of Takeuchi. Thus, if we can detect cryoconite in satellite images, we can correct for its effects on the water depth calculations. Areas of cryoconite are occasionally large enough to be detected in satellite images as can be seen in Figure 1, an ASTER image with 15 m spatial resolution. In the case of Figure 1 it is a simple matter to mask out the cryoconite pixels before calculating the water depth and volume in this subimage.

For pixels that might contain a mixture of cryoconite and water, spectral mixture analysis (SMA) can determine the fractions of each in a pixel (Adams and others, 1995; Tompkins and others, 1997). The Tompkins and others (1997) method is especially useful because it requires no prior knowledge of the spectra of the components that might mix in a pixel. Nevertheless, the

spectral analyses of Takeuchi and colleagues can provide good intial values for determining the endmembers. The use of SMA in conjuction with the depth algorithm of Sneed and Hamilton (2007) is the next step in the ongoing refinement of the algorithm.

Dark and deep water

R_∞, reflectance over optically deep water where the influence of bottom reflectance is nil, can be derived from water that is deeper than ∼40 m and is one of the two end points needed to solve Equation 2, the other being A_d, bottom or substrate albedo (reflectance). To test the sensitivity of volume calculations to the value of R_∞ and to investigate whether it is necessary that the image containing meltwater also contain deep water pixels, 10 widely scattered (in space and time) ASTER images with deep ocean water were used to extract small, VNIR1 subimages (∼30-by-30 pixels) of only deep water. Two images are from northwestern Greenland, four from northeastern Greenland, one from southeastern Greenland, and three from eastern and southeastern Svalbard. One of the northeastern Greenland images is an ascending pass and the southeastern Greenland image has a low gain setting for VNIR1 rather than a normal gain setting. The ten subimages were corrected to provide top-of-atmosphere reflectance and the minimum digital number (DN) value in each subimage was determined (Table 2). An atmospherically corrected ASTER scene from 13 July 2004 of the ice cap, Austfonna, located on the island of Nordaustlandet, Svalbard, was used to calculate the meltwater volume. Only one of the ten R_∞ subimages was derived from this 13 July 2004 image and its R_∞ value was used in trial 1 (Table 2) to calculate the meltwater volume.

The DN values in Table 2 were recorded so that they might act as a guide in choosing subimages of deep ocean water that would, in turn, provide an accurate endpoint for R_∞ in Equation 2. The median DN value for trials 2–11 is 16, the median volume is 5.73x10^6 m^3, and the median % difference is 2.0%. If we exclude outliers, trials 5 and 6, the medians become 14, 5.69x10^6 m^3, and 1.2%, respectively. A close examination of the images used in Trials 5 and 6 using the thermal infrared bands revealed that high, thin clouds covered both images used for R_∞. The only clear but not surprising pattern to emerge from Table 2 is that deep water subimages with low DN values and closer to the DN value of the first trial produce volumes with the smallest percentage of volume change relative to the first or basis trial.

The deep water subimages for trials 2, 3, 7, and 9 (those trials with the smallest % difference relative to trial 1) are from northeastern Svalbard, southeastern Svalbard, northeastern Greenland, and northeastern Greenland, respectively. The image dates for these four trials are 07 July 2004, 04 July 2005, 21 August 2000, and 21 July 2003, respectively.

It is difficult to account for the considerable variation in % difference between trials 3 and 8 which both have the same DN value. They are widely separate in space and time — southeastern Svalbard and northeastern Greenland and 04 July 2005 and 10 August 2000, respectively. Trial 8's subimage does have the largest off-nadir pointing angle (-8.575°) of all the trials. However, there are not enough images with varying pointing angles to attempt an analysis of its effect on the calculated volume. It seems reasonable to conclude, based on the foregoing, that it is unnecessary to use an image that contains deep

ocean water in order to calculate surface meltwater volume nor does it matter when or where the deep water subimage (thus, R_∞) is obtained so long as care is taken to select water with DN values of 11–14.

A similar test using Landsat 7 ETM+ images has not been undertaken nor has one using MODIS images. A variable viewing angle is not an issue with Landsat however gain settings can vary depending on surface type and sun elevation angle (Irish, 1999). Given the large number of MODIS data products, the key consideration is to use one that is not a composite of daily orbits, pointing angles, and gain settings (e.g., MOD02). As with ASTER images, care should be exercised when choosing "blackest" deep water pixels

NUMERICAL MODELING

A simple modeling exercise was carried out that compared the deepest depth derived using Equation 2 with that calculated by HYDROLIGHT® (Sequoia Scientific, Inc., Bellevue, WA, USA), a radiative transfer numerical modeling software. In situ, laboratory, and satellite data provided the input parameters to HYDROLIGHT®. Additional model inputs of total ozone, column precipitable water vapor, and surface pressure data were taken from MODIS, the MOD07 Atmospheric Profile data product for 11 July 2008. The maximum depth calculated by Equation 2 was 4.2 m while the modeled maximum depth (using the Petzold average particle phase function (Mobley, 2004)) was 4.1m, a difference of ∼2.4%.

CONCLUSIONS

When using the method for determining water depth set out in Sneed and Hamilton (2007) and Equation 1, it is reasonable to assume that inelastic scattering plays no part in that calculation while wind-generated surface waves have a very small effect on the derived depth. Furthermore, we have demonstrated that it is not necessary that the satellite image showing surface meltwater must also contain dark, infinitely deep water as well. Based on three years of water analyses of meltwater from eastern Greenland we are confident that dissolved or suspended particulate matter plays a minor role in accurately determining meltwater depth and volume. Nevertheless, a larger sample set would be welcome and we will continue to collect and analyze meltwater from different regions of Greenland. The assumption of substrate homogeneity remains somewhat problematic and warrants further investigation. Spectral mixture analysis may provide a method for determining what percentage of a pond's substrate with a different albedo from that of ice would significantly effect the derived depth and volume.

Given 30 m resolution of Landsat 7 ETM+, in situ measured water depths agree reasonably well with those derived from a Landsat image with the greatest depths found near the center of the pond and the shallowest at the edges. The numerically modeled maximum depth agrees very closely with that from the Landsat image.

ACKNOWLEDGEMENTS

GSH is supported by NASA's Cryospheric Sciences Program and WAS is supported by a NASA Earth and Space Science Fellowship. From the School of Marine Sciences, Univ. of Maine Dr. E. Boss for the loan of radiometers, access to Hydrolight, and discussions and Dr. C. Roesler, Mr. W. Slade, and Ms M. Estapa for the optical analyses of water samples. From the Climate Change Institute, Univ. of Maine Ms S. B. Sneed for chemical analysis of water samples and Dr. J. Saros for the loan of an inflatible research vessel..

REFERENCES

Adams, J. B., D. E. Sabol, V. Kapos, R. A. Filho, D. A. Roberts, M. O. Smith and A. R. Gillespie, 1995. Classification of Multispectral Images Based on Fraction of Endmembers: Application to Land-Cover Change in the Brazilian Amazon, *Remote Sensing of Environment*, **52**, 137–154.

Babin, M., A. Morel, V. Fournier-Sicre, F. Fell and D. Stramski, 2003. Light scattering properties of marine particles in coastal and ocean waters as related to the particle mass concentration, *Limnology and Oceanography*, **48**(2), 843–859.

Bartholomew, I., P. Nienow, D. Mair, A. Hubbard, M. A. King and A. Sole, 2010. Seasonal evolution of subglacial drainage and acceleration in a Greenland outlet glacier, *Nature Geoscience*, **3**, 408–411.

Bøggild, C. E., R. E. Brandt, K. J. Brown and S. G. Warren, 2010. The ablation zone in northeast Greenland: ice types, albedos and impurities, *Journal of Glaciology*, **56**(195), 101–113.

Boon, S. and M. Sharp, 2003. The role of hydrologically-driven ice fracture in drainage system evolution on an Arctic glacier, *Geophysical Research Letters*, **30**(18), 1916.

Boss, E., M.S. Twardowski and S. Herring, 2001. Shape of the particulate beam attenuation spectrum and its inversion to obtain the shape of the particulate size distribution, *Applied Optics*, **40**(27), 4885–4893.

de Caritat, P., G. Hall, S. Gìslason, W. Belsey, M. Braun, N.I Goloubeva, H. K. Olsen, J. O. Scheie and J. E. Vaive, 2005. Chemical composition of arctic snow: concentration levels and regional distribution of major elements, *Science of the Total Environment*, **336**, 183–199.

Das, S.B., I. Joughin, M.D. Behn, I.M. Howat, M.A. King, D. Lizarralde and M.P. Bhatia, 2008. Fracture Propagation to the Base of the Greenland Ice Sheet During Supraglacial Lake Drainage, *Science*, **320**(5877), 778–781.

Davies-Colley, R.J., 1983. Optical properties and reflectance spectra of 3 shallow lakes obtained from a spectrophotometric study, *New Zealand Journal of Marine and Freshwater Research*, **17**, 445–459.

Gadja, R. T., 1958. Cryoconite phenomena on the Greenland ice cap in the Thule area, *The Canadian Geographer*, **3**(12), 35–44.

Gerdel, R. W. and F. Drouet, 1960. The Cryoconite of the Thule Area, Greenland, *Transactions of the American Microscopical Society*, **79**(3), 256–272.

Gordon, H. R., 1999. Contribution of Raman scattering to water-leaving radiance: a reexamination, *Applied Optics*, **38**(15), 3166–3174.

Irish, Richard, 1999. Landsat 7 Science Data Users Handbook, Landsat Project Science Office, Goddard Space Flight Center.

Joughin, I., S.B. Das, M.A. King, B.E. Smith, I.M. Howat and T. Moon, 2008. Seasonal speedup along the western flank of the Greenland Ice Sheet, *Science*, **320**, 781–783.

Legrand, M. and P. Mayewski, 1997. Glaciochemistry of Polar ice cores: A Review, *Reviews of Geophysics*, **35**(3), 219–243.

Lemke, P., J. Ren, R. B. Alley, I. Allison, J. Carrasco, Y. Fujii, G. Kaser, P. Mote, R. H. Thomas and T. Zhang, 2007. Observations: Changes in Snow, Ice, and Frozen Ground, Solomon, S.D., D. Qin, M. Manning, Z. Chen, M. Marquis, K.B. Averyt, M. Tignor and H.L. Miller, eds., Climate Change 2007: The Physical Science Basis. Contributions of Working Group I to the Fourth Assessment Report of the Intergovernmental Panel on Climate Change, Cambridge University Press, chap. 4, 339–383.

Meehl, G.A., T.F. Stocker, W.D. Collins, P. Friedlingstein, A.T. Gaye, J.M. Gregory, A. Kitoh, R. Knutti, J.M. Murphy, A. Noda, S.C.B. Raper, I.G. Watterso, A.J. Weaver and Z.-C. Zhao, 2007. Global Climate Projections, Solomon, S.D., D. Qin, M. Manning, Z. Chen, M. Marquis, K.B. Averyt, M. Tignor and H.L. Miller, eds., Climate Change 2007: The Physical Science Basis. Contributions of Working Group I to the Fourth Assessment Report of the Intergovernmental Panel on Climate Change, Cambridge University Press, chap. 10, 749–846.

Mobley, Curtis D., 2004. Light and Water: Radiative Transfer in Natural Waters, C. D. Mobley, CD-ROM ed.

Parizek, B.R. and R.B. Alley, 2004. Implications of increased Greenland surface melt under global-warming scenarios: ice-sheet simulations, *Quaternary Science Reviews*, **23**, 1013–1027.

Philpot, W. D., 1989. Bathymetric mapping with passive multispectral imagery, *Applied Optics*, **28**(8), 1569–1578.

Pilson, M. E. Q., 1998. An Introduction to the Chemistry of the Sea, Prentice Hall.

Shepherd, A., A. Hubbard, P. Nienow, M. King, M. McMmillan and I. Joughin, 2009. Greenland ice sheet motion coupled with daily melting in late summer, *Geophysical Research Letters*, **36**, L0150.

Smith, R. C. and K. S. Baker, 1981. Optical properties of the clearest natural waters (200-800 nm), *Applied Optics*, **20**(2), 177–184.

Sneed, W. A. and G. S. Hamilton, 2007. Evolution of melt pond volume on the surface of the Greenland Ice Sheet, *Geophysical Research Letters*, **34**(doi:10.1029/2006GL028697).

Takeuchi, N., 2002a. Optical characteristics of cryoconite (surface dust) on glaciers: relationship between light absorbency and the property of organic matter contained in the cryoconite, *Annals of Glaciology*, **34**, 409–414.

Takeuchi, N., 2002b. Surface albedo and characterisitics of cryoconite (biogenic surface dust) on an Alaskan glacier, Gulkana Glacier in the Alaska Range, *Bulletin of Glaciological Research*, **19**, 63–70.

Takeuchi, N., S. Kohshima and T. Segawa, 2003. Effect of cryoconite and snow algal communities on the surface albedo of maritime glaciers in south Alaska, *Bulletin of Glaciological Research*, **20**, 21–27.

Takeuchi, N., S. Kohshima, T. Shiraiwa and K. Kubota, 2001. Characteristics of cryoconite (surface dust on glaciers) and surface albedo of a Patagonian glacier, Tyndall Glacier, Southern Patagonia Icefield, *Bulletin of Glaciological Research*, **18**, 65–69.

Takeuchi, N. and Z. Li, 2008. Characteristics of Surface Dust on the Ürümqi Glacier No. 1 in the Tien Shan Mountains, China, *Arctic, Antarctic, and Alpine Research*, **40**(4), 744–750.

Tompkins, S., J. F. Mustard, C. M. Pieters and D. W. Forsyth, 1997. Optimization of Endmembers for Spectral Mixture Analysis, *Remote Sensing of Environment*, **59**, 472–489.

Van der Veen, C. J., 2007. Fracture propagation as means of rapidly transferring meltwater to the base of glaciers, *Geophysical Research Letters*, **34**(doi:10.1029/2006GL028385).

Van de Wal, R.S.W., W. Boot, M.R. van den Broeke, C.J.P.P. Smeets, C.H Reijmer, J.J.A. Donker and J. Oerlemans, 2008. Large and rapid melt-induced velocity changes in the ablation zone of the Greenland Ice Sheet, *Science*, **321**, 111–113.

Vermote, E., D. Tanrè, J. L. Deuzè, M.Herman, J. J. Morcette and S. Y. Kotchenova, 2005. Second Simulation of a Satellite Signal in the Solar Spectrum - Vector (6SV), NASA-Goddard Space Flight Center, Greenbelt, MD 20771, USA.

Zaneveld, J. R. V., E. Boss and P. A. Hwang, 2001. The influence of coherent waves on the remotely sensed reflectance, *Optics Express*, **9**(6), 260–266.

Zwally, H.J., W. Abdalati, T. Herring, K. Larson, J. Saba and K. Steffen, 2002. Surface melt induced acceleration of Greenland Ice Sheet flow, *Science*, **297**, 218–222.

Table 1. Shallow water wave amplitude as a function of wind speed, fetch, and water depth.

Wind speed m^{-1}	Fetch km	Water depth m	Wave amplitude m	Wavelength m
2	0.5	15	0.019	0.47
2	1.0	15	0.026	0.68
20	0.5	15	0.32	3.5
20	1.0	15	0.45	5.5
20	2.0	30	0.64	8.7

Table 2. R_∞ vs. volume, Austfonna, Nordaustlandet, Svalbard.

Trial	DN Value	13 July 2004 Volume (10^6 m^3)	% Difference* of Volume
1	14	5.62	n/a
2	14	5.61	-0.2
3	16	5.62	0.0
4	17	5.65	+0.5
5	43	7.41	+31.9
6	26	6.19	+10.1
7	11	5.69	+1.2
8	16	5.91	+5.2
9	14	5.69	+1.2
10asc	11	5.77	+2.7
11low	19	5.93	+5.5

*Difference in volume relative to Trial #1

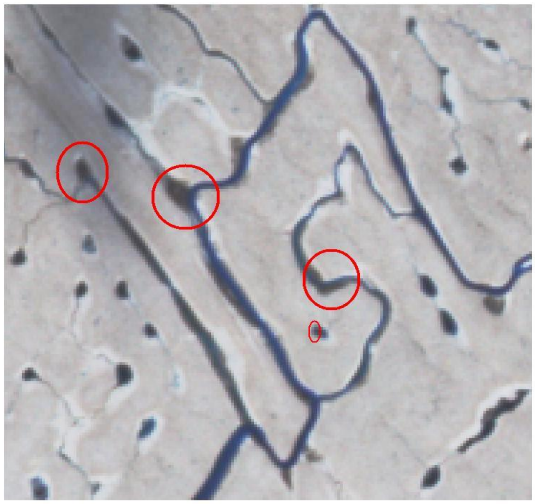

Fig. 1. A portion of an ASTER image (05 August 2009) of the Nioghalvfjerdsfjorden Glacier ice tongue, northeast Greenland, near the terminus. Red ellipses outline areas of cryoconite.

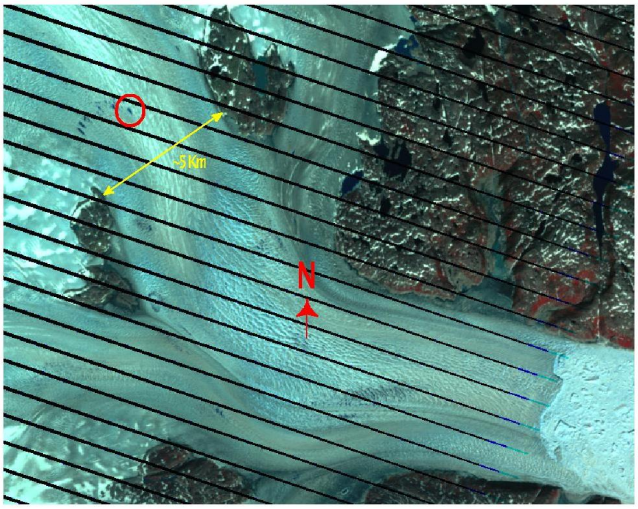

Fig. 2. A portion of the 20 July 2008 Landat 7 image showing the melt ponds on Helheim Glacier, east Greenland. The red ellipse indicates the pond where the 11 July 2008 measurements were made.

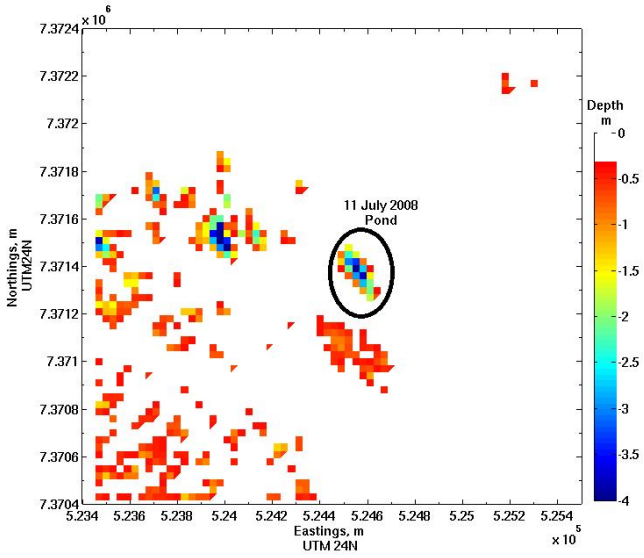

Fig. 3. A water depth map of the melt pond where the July 11th measurements were made.